https://doi.org/10.5194/egusphere-2026-4214
Preprint. Discussion started: 11 August 2026

MJO unlocks the stratospheric polar vortex influence on winter extreme precipitation over South China

Fang Zhou[1, 2*], Shuo Han[1], Zhicong Yin[1], Tingting Han[1], and Dingzhu Hu[1]

[1]*State Key Laboratory of Climate System Prediction and Risk Management/Key Laboratory of Meteorological Disaster, Ministry of Education/Collaborative Innovation Center on Forecast and Evaluation of Meteorological Disasters, School of Atmospheric Sciences, Nanjing University of Information Science and Technology, Nanjing 210044, China*

[2]*The Institute of Atmospheric Environment/Northeast China Cold Vortex Research Key Laboratory, China Meteorological Administration, Shenyang 110002, China*

**Correspondence to:* Fang Zhou (zhouf@nuist.edu.cn)

https://doi.org/10.5194/egusphere-2026-4214
Preprint. Discussion started: 11 August 2026

Abstract

Winter extreme precipitation over South China (SC) exerts profound impacts, yet its stratospheric drivers remain limited understood, with a long-standing puzzle of the statistically weak linkage between the stratospheric polar vortex (SPV) and SC rainfall extremes. Here, using observational analyses and CMIP6 historical simulations, we demonstrate that a Eurasia-shifted SPV (ESSPV) can increase SC winter extreme precipitation, but this modulation is strictly phase-locked to the Madden–Julian Oscillation (MJO), occurring predominantly during MJO phases 2–5. Two synergistic pathways explain this phenomenon. First, the ESSPV excites a Rossby wave across Eurasia, inducing a low-level northeasterly anomaly north of SC that strengthens local moisture convergence. Second, the ESSPV couples with the westerly quasi-biennial oscillation (WQBO), which amplifies the MJO-associated anomalous anticyclone over the western North Pacific and enhances low-latitude moisture transport toward SC. CMIP6 multi-model analyses further confirm that the fidelity of MJO phase 2–5-associated western North Pacific anticyclone determines a model's ability to reproduce the observed linkage, firmly establishing the MJO as the indispensable gateway linking the SPV to SC extreme precipitation.

1 Introduction

Against the background of global warming, the frequency, intensity, and duration of extreme precipitation events have increased markedly across the globe (IPCC, 2021) , triggering severe floods, secondary geological disasters, and enormous losses to human lives, socioeconomic assets, and ecosystems (Huang et al., 1998; Zhu et al., 2016; Zhou et al., 2021; Zhang et al., 2017). South China (SC), located in the core of the Asian monsoon region, is a hotspot of extreme precipitation with exceptionally high climate vulnerability (Yin et al., 2019). A series of catastrophic winter precipitation extremes have struck SC in recent years. For example, the 2015 winter flood affected 1.407 million residents and caused direct economic losses of $249 million, the February 2022 severe ice-snow disaster impacted 7.314 million people with $1.2 billion in direct losses, and the April 2024 extensive flood ravaged more than 140,000 hectares of crops and inflicted $1.797 billion in economic losses (National Disaster Reduction Center of China, https://www.ndrcc.org.cn; Ministry of Emergency Management of the People's Republic of China, https://www.mem.gov.cn). Improving the understanding of drivers and physical mechanisms underlying SC winter extreme precipitation is therefore critical for regional climate prediction and disaster prevention (Bao et al., 2010; Gao et al., 2009).

Existing research on SC winter precipitation variability and extremes has predominantly focused on tropospheric dynamics and air–sea interactions, including the El Niño–Southern Oscillation (ENSO) (Rao et al., 2019; Alexander et al., 2002a, 2002b), Atlantic and Indian Ocean sea surface temperature (SST) anomalies (Han and Zhang, 2022; Zhu et al., 2024), the South Asian High (Liu et al., 2013; Wei et al., 2015), the western North Pacific Subtropical High (Zhou et al., 2024), thermal forcing of the Qinghai-Tibet Plateau (He et al., 2019; Lu et al., 2023), and Arctic sea ice loss (Zhang, 2015). However, the subseasonal-to-seasonal prediction of winter precipitation remains a long-standing challenge (Rivoire et al., 2023; DeFlorio et al., 2019; Zhang

https://doi.org/10.5194/egusphere-2026-4214
Preprint. Discussion started: 11 August 2026

et al., 2024), largely due to incomplete understanding of cross-scale and cross-layer dynamical couplings. In recent years, the stratosphere has emerged as a critical source of predictability for Northern Hemisphere surface climate (Rao et al., 2025; Zhang et al., 2026). As the dominant stratospheric circulation system, the stratospheric polar vortex (SPV) exerts profound and persistent impact on mid-to-high latitudes via stratosphere–troposphere interaction (Zhang et al., 2022; Hu et al., 2024, 2025). While numerous studies have documented a robust linkage between SPV variability and cold air outbreaks over East Asia (Baldwin et al., 2021; Zhang et al., 2019; Yu et al., 2018, 2019), its influence on extreme precipitation remains severely understudied. The few relevant investigations are mostly limited to individual case studies, primarily because the SPV–extreme rainfall relationship is statistically weak and unstable in the climatological sense (Wang et al., 2025). This gap motivates a fundamental reconsideration of the necessary conditions for extreme precipitation occurrence. Since extreme rainfall requires both sufficient low-latitude moisture transport and strong local dynamical convergence, yet the SPV is a cold, dry polar system that cannot independently supply the essential moisture, we hypothesize that the SPV's influence on extreme precipitation is "locked" behind a hidden moisture pathway.

The Madden–Julian Oscillation (MJO), the dominant mode of tropical intraseasonal variability, has long been recognized as a primary driver of winter monsoon precipitation variability (Madden and Julian, 1971, 1994; Shimizu et al., 2017; Jia et al., 2011; Garfinkel et al., 2014) and a core source of subseasonal-to-seasonal predictability for extreme events (Peng et al., 2024; Kim et al., 2023; Liu et al., 2024; Dey et al., 2020). Through its eastward-propagating convective activity, the MJO modulates tropical and subtropical circulations, exerting pronounced impacts on rainfall distribution over East Asia (Schreck, 2021; Wang et al., 2022; Chen et al., 2020). Notably, the MJO is more active during boreal winter and exerts stronger modulation on winter precipitation across multiple timescales compared to summer (Yao et al., 2015). Given its critical role in delivering low-latitude moisture, the MJO is a natural candidate to provide the missing moisture pathway. However, few studies have recognized the MJO's potential to unlock the puzzle of the weak SPV–extreme precipitation linkage. In this study, we first establish the interannual linkage between the SPV and extreme precipitation, then reveal the strict phase dependence of this linkage on the MJO, and further elucidate the synergistic dynamical pathways underpinning this phenomenon. Multiple coupled climate models from the Coupled Model Intercomparison Project Phase 6 (CMIP6) are further employed to demonstrate the decisive factor for reproducing the observed SPV–extreme precipitation linkage.

2 Data and Methods

2.1 Reanalysis and CMIP6 simulation datasets

Two precipitation datasets were utilized in this study: (a) the Global Precipitation Climatology Project (GPCP) dataset (Adler et al., 2018), providing daily precipitation on 1° × 1° grids from 1996 to present; (b) the CN05.1 dataset from the China Meteorological Administration, offering daily precipitation on 0.25° × 0.25° grids from 1979 to 2022 (Wu and Gao, 2013). Daily and monthly atmospheric variables were sourced from the National Centers for Environmental

Prediction–Department of Energy (NCEP–DOE) reanalysis 2 (Kanamitsu et al., 2002), available from 1979 to the present on 2.5° × 2.5° grids. Daily mean outgoing longwave radiation (OLR) data were obtained from the National Oceanic and Atmospheric Administration (NOAA) interpolated OLR dataset (Liebmann et al., 1996). Monthly mean sea surface temperature (SST) data were obtained from the NOAA Extended Reconstructed Sea Surface Temperature version 5 (ERSST v5) (Huang et al., 2017), covering the period 1979 to 2022.

Historical simulations from 27 coupled climate models participating in the CMIP6 were used (Table S1) (Eyring et al., 2016). The analysis period spans 1964–2014. Model data were interpolated onto a standardized 2.5° × 2.5° grid using bilinear interpolation. Quadratic linear trends were removed from all datasets to mitigate the potential influences of global warming. Leap days were omitted from all datasets, as most CMIP6 models use a 365-day calendar. To eliminate the interference of each model's intrinsic climatology, model anomalies were computed relative to the observational and reanalysis climatology over the common reference period 1981–2010.

2.2 Methods

Winter extreme precipitation was defined as daily rainfall exceeding the 90th percentile of all winter rainy days during November to March (NDJFM), denoted as R90 (Zhang et al., 2011). The ESSPV index was defined as the regionally averaged 50-hPa geopotential height anomaly over the Eurasian sector (50°N–80°N, 20°E–100°E). ESSPV winters were defined as those with a standardized NDJFM SPV index lower than −0.7, and EWSPV winters as those with an index greater than 0.7. During the analysis period, 13 ESSPV winters and 13 EWSPV winters were identified (Table S2). The MJO indices were derived from the first two principal components of a multivariate empirical orthogonal function analysis of 30–60-day filtered OLR, 200-hPa, and 850-hPa zonal wind anomalies over the tropics (15°S–15°N). To ensure spatiotemporal consistency, the corrected combined anomaly fields from each CMIP6 model were projected onto the spatial pattern of the MJO mode derived from reanalysis data to obtain the simulated MJO indices. The MJO was classified into eight phases based on the phase angle, and only events with a normalized MJO amplitude exceeding 1.0 standard deviation were retained. To examine whether the ESSPV influence is linearly related to ENSO, the Niño3.4 index (area-averaged SST anomaly over 5°S–5°N, 170°W–120°W during NDJFM) was used to represent ENSO variability, and its linear signal was regressed out from all variables prior to analysis

3 Interannual linkage between SPV and extreme precipitation

Since SC exhibits the largest variability in both winter total precipitation and extreme precipitation across China (Figure S1), this region is considered highly sensitive to climate variability. Hence, we begin by examining the statistical association between the stratosphere and SC extreme precipitation. Regression of boreal winter (November to March) mean 50-hPa geopotential height anomalies onto the regionally averaged R90 (defined as daily rainfall exceeding the 90th percentile of all winter rainy days, see Methods) anomaly over SC (21°–29°N, 107°–122°E) shows that a Eurasia-shifted stratospheric polar vortex (ESSPV) corresponds to

https://doi.org/10.5194/egusphere-2026-4214
Preprint. Discussion started: 11 August 2026

increased extreme precipitation over SC (Figure 1a). Over two-thirds of the SPV negative geopotential height anomaly body is located in the Eastern Hemisphere, with the high-correlation region centered near the Ural Mountains. However, this shift lacks statistical significance, exposing a fragile SPV–extreme precipitation linkage at the winter-mean scale. A singular value decomposition (SVD) analysis further corroborates the ESSPV–increased SC R90 relationship, with the leading mode explaining 85.9% of the total coupled variance. Yet the temporal correlation between the corresponding expansion coefficients is only 0.35, reinforcing the concern that the SPV–extreme precipitation connection is statistically non-robust (Figure S2).

Likewise, defining the ESSPV index as the area-averaged 50-hPa geopotential height anomaly over the Eurasian sector (50°–80°N, 20°–100°E) and regressing extreme precipitation onto this standardized index offers a reciprocal perspective. The regressed R90 pattern supports a potential interannual linkage whereby an ESSPV tends to be accompanied by increased extreme precipitation over SC (Figures 1f, g). Notably, this ESSPV index correlates with the concurrent Niño3.4 index at merely −0.17, suggesting that the linkage is linearly independent of ENSO. Yet the scatter plot of the ESSPV index against SC R90 shows considerable dispersion (Figure 1h). While the mean R90 is generally higher under ESSPV conditions and lower under Eurasia-withdraw SPV (EWSPV) conditions, the correlation coefficient reaches only −0.27, still lacking statistical robustness.

To explore the dynamical pathways linking the ESSPV to extreme precipitation, we conduct regression analyses of atmospheric circulations onto the ESSPV index. The results reveal a clear Rossby wave train excited by the ESSPV, propagating downstream across Eurasia in the upper troposphere (Figure 1b) and characterized by an anomalous anticyclone over eastern Siberia (Figure 1c). This anticyclone induces pronounced cold, dry northeasterly anomalies in the lower troposphere over eastern China (Figure 1d), which enhance the thermal contrast between cold northern air and warm moist southern air and strengthen low-level moisture convergence over SC. The pressure–latitude cross section of zonal wind associated with the ESSPV index further shows that the ESSPV is characterized by deep westerly anomalies extending from the stratospheric polar region downward to the lower troposphere (Figure 1e). Under the Holton–Tan framework, the SPV is preferentially coupled with the phase of the quasi-biennial oscillation (QBO): 10 out of 13 ESSPV winters correspond to the westerly QBO (WQBO) phase, while 9 out of 13 EWSPV winters correspond to the easterly QBO (EQBO) phase (Table S2). The WQBO-associated tropical stratospheric westerly anomalies arch downward into the lower troposphere, enhancing the background subtropical westerlies over the India–Indochina Peninsula (Figures 1c, d). Additionally, a tropical tropospheric easterly anomaly, arising from the downward propagation of the preceding EQBO phase, is embedded within the alternating QBO zonal wind cycle (Figure 1e). Probability density distributions further confirm the interannual coupling among ESSPV, WQBO, and enhanced SC R90, in contrast to the EWSPV–EQBO–reduced SC R90 configuration (Figure S3).

Thus, the ESSPV provides a physically credible large-scale circulation background for SC extreme precipitation via two distinct preliminary pathways: a high-latitude Rossby wave train that enhances local dynamical convergence, and a tropical-stratospheric pathway via Holton–Tan

https://doi.org/10.5194/egusphere-2026-4214
Preprint. Discussion started: 11 August 2026

coupling with the WQBO that strengthens subtropical westerlies. Yet this background does not translate into a strong statistical linkage at the winter-mean scale, because a favorable seasonal-mean state alone cannot directly trigger extreme precipitation events. This disconnect motivates us to further explore the intraseasonal dynamical processes that may unlock the SPV's influence on extreme rainfall.

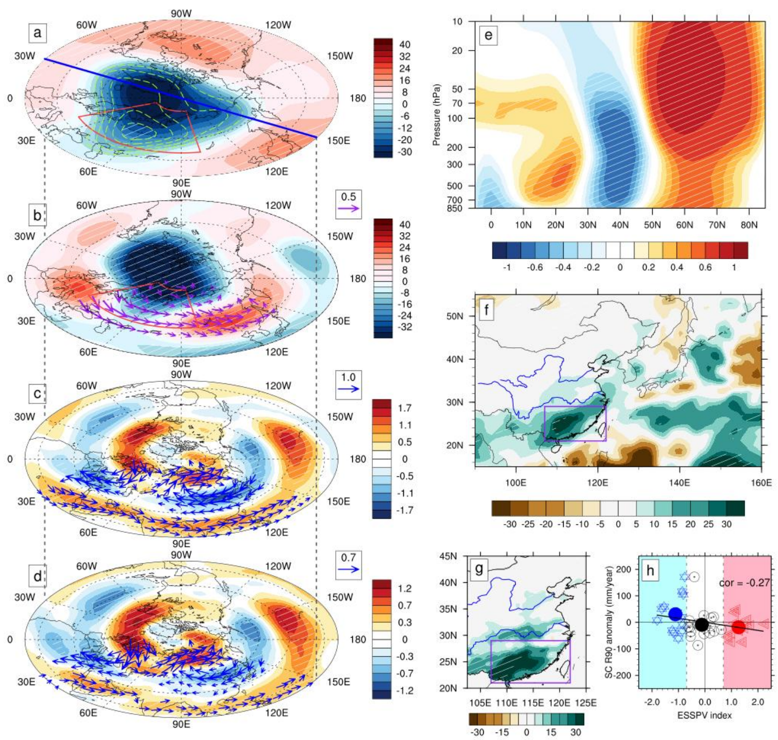

Figure 1 | Circulation background and responses of extreme precipitation over South China under SPV modulation. a. Regressed NDJFM mean 50-hPa geopotential height anomalies (shading, unit: gpm) and correlation coefficients (green dashed contours; interval −0.05, starting from −0.1) onto the regionally averaged R90 anomaly over SC. White slashes indicate regressed geopotential height anomalies significant at the 95% confidence level. **b.** Regressed NDJFM mean 200-hPa geopotential height anomalies (shading, unit: gpm) and wave activity flux (vectors, unit: $m^2\ s^{-2}$) onto the ESSPV index (multiplied by −1). White slashes indicate significant geopotential height anomalies at the 95% confidence level. **c–d.** Same as **b**, but for (**c**) 500-hPa and (**d**) 700-hPa horizontal wind anomalies (vectors, unit: m s^{-1}, only those significant at the 95% confidence level are shown) and the zonal wind component (shading, unit: m s^{-1}). White slashes indicate significant zonal wind anomalies at the 95% confidence level. **e**. Pressure–latitude cross section of correlation coefficients between the zonal wind anomalies averaged over 30°W–150°E and the ESSPV index. White slashes indicate significant correlation coefficients at the 95% confidence level. **f–g.** Same as **b**, but for (**f**) GPCP and (**g**) CN05.1 R90 anomalies (shading, unit:

mm). White slashes denote significant R90 anomalies at the 95% confidence level. **h.** Scatter plot of the normalized NDJFM ESSPV index versus regionally averaged R90 over SC. The correlation coefficient is shown in the panel. Blue, red, and black dots indicate ESSPV, EWSPV, and neutral winters, respectively. Large solid dots represent the mean values. The red and purple boxes denote the ESSPV (50°–80°N, 20°–100°E) and SC (21°–29°N, 107°–122°E) domains, respectively.

4 Role of MJO in the impact of Eurasia-shifted SPV on extreme precipitation

The seasonal-mean background associated with the ESSPV only provides a favorable precondition for SC extreme precipitation, rather than directly triggering extreme rainfall events. This explains why the SPV–SC extreme precipitation linkage remains statistically weak in the climatology, and leads us to hypothesize that intraseasonal variability acts as the critical key that unlocks the SPV's influence. To test this, we examine the periodicity of daily precipitation anomalies over SC during ESSPV and EWSPV winters. The results show that SC precipitation exhibits a dominant intraseasonal periodicity of 30–60 days, with significantly stronger spectral power during ESSPV winters than during EWSPV winters (Figure 2a, Figure S4). This 30–60-day periodicity matches the characteristic timescale of the MJO, strongly suggesting that the MJO mediates the linkage between the interannual ESSPV background and intraseasonal rainfall extremes over SC.

Composite precipitation anomalies across all eight MJO phases under ESSPV and EWSPV backgrounds confirm the MJO's phase-dependent modulation of the SPV–extreme precipitation linkage. Relative to EWSPV winters, SC precipitation during MJO phases 2–5 is markedly enhanced under the ESSPV background, whereas no consistent enhancement is observed during phases 6–8 and 1 (Figure 2b, Figure S5). Probability density distributions of regionally averaged SC precipitation further validate this phase dependence: during MJO phases 2–5, the 90th, 75th, and 50th percentiles, as well as the mean daily precipitation over SC, are heavily skewed toward higher values in ESSPV winters than in EWSPV winters (Figure 2c). Notably, the amplitude of MJO phases 2–5 is actually weaker under the ESSPV background than under the EWSPV background (solid dot octagons in Figure 2c, Figure S6), likely because the WQBO associated with the ESSPV generates a warm temperature anomaly near the tropical tropopause, whose enhanced static stability suppresses the upward development of MJO deep convection (Green and Furtado, 2019; Liu et al.,2014; Martin et al., 2021). Yet, despite this reduced convective intensity, MJO phases 2–5 under the ESSPV background still yield a significantly higher probability of extreme precipitation occurrence than the same phases under EWSPV conditions, using the 90th percentile as the extreme rainfall threshold. This "weaker MJO intensity–stronger extreme precipitation" paradox firmly establishes that the ESSPV amplifies SC extreme precipitation not by strengthening the MJO itself, but by enhancing its teleconnection and circulation response, thereby positioning the MJO as the indispensable key that unlocks the SPV–extreme precipitation linkage, with this amplification almost exclusively restricted to MJO phases 2–5.

https://doi.org/10.5194/egusphere-2026-4214
Preprint. Discussion started: 11 August 2026

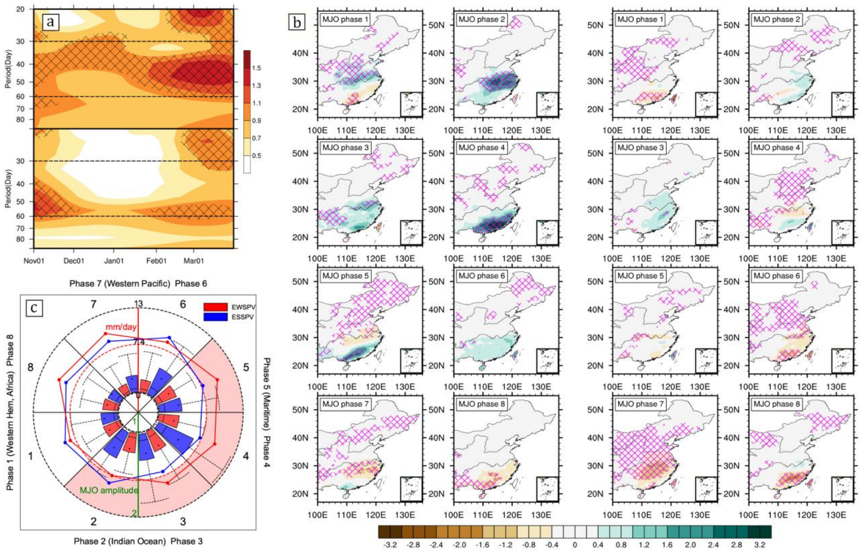

Figure 2 | Precipitation responses under the synergistic impacts of ESSPV and MJO. a. Mean wavelet spectra of the regionally averaged daily precipitation anomalies over SC for each ESSPV (top) and EWSPV (bottom) winter. Time labels on the bottom x-axis represent the 1st day of each month. Black meshes indicate the 95% confidence level. **b.** Composite evolution patterns of MJO phases 1–8 precipitation anomalies (unit: mm day^{-1}) associated with ESSPV (left) and EWSPV (right) winters. Meshes indicate significant precipitation anomalies at the 95% confidence level. **c.** Probability density distributions of daily precipitation in SC during MJO phases 1–8 in ESSPV (blue box) and EWSPV (red box) winters. The box bounds indicate the 10th, 25th, 50th, 75th, and 90th percentiles, and dots indicate the mean. The solid dot octagons denote the average amplitude of MJO in ESSPV (blue) and EWSPV (red) winters. The red dashed line indicates the wintertime 90th percentile threshold for SC precipitation (about 7.4 mm day^{-1}).

To elucidate the synergistic dynamical mechanism of the ESSPV and MJO in amplifying SC extreme precipitation, we composite the vertically integrated water vapor flux and its divergence, as well as the 850-hPa horizontal winds and their divergence, under different SPV backgrounds during MJO phases 2–5 (Figure 3). Under climatological conditions, MJO phases 2–5 are characterized by enhanced convection over the tropical Indian Ocean and Maritime Continent. The tropical easterly inflows on the eastern flank of this convection curl northward into the subtropics, forming an anomalous anticyclone over the western North Pacific that transports abundant moisture from the low-latitude ocean toward SC, resulting in above-normal precipitation (Figures 3a, d).

Under the ESSPV regime, two pronounced changes emerge. First, the MJO-associated anomalous anticyclone over the western North Pacific is significantly reinforced. This intensification is linked to the WQBO phase that accompanies the ESSPV, which strengthens the tropical easterlies and subtropical westerlies in the troposphere, thereby amplifying moisture

https://doi.org/10.5194/egusphere-2026-4214
Preprint. Discussion started: 11 August 2026

transport and convergence over SC (Figure 3b). Second, this western North Pacific anticyclone and the ESSPV-induced anomalous anticyclone over eastern Siberia confront each other, creating a sharp wind-field contrast between low-latitude southwesterlies and high-latitude northeasterlies that further enhances convergence and upward motion (Figure 3e). Although the MJO itself weakens under the ESSPV background, the two processes associated with its remote anticyclonic response together make extreme precipitation over SC substantially more likely.

During EWSPV winters, the western North Pacific anticyclone weakens, suppressing moisture transport (Figure 3c). Moreover, the anomalous circulation over eastern Siberia shifts to cyclonic; the weakened low-latitude southwesterlies are met by high-latitude southwesterly anomalies, providing little contribution to convergence and upward motion (Figure 3f). Consequently, even during MJO phases 2–5, which are otherwise favorable for SC precipitation, the EWSPV background suppresses rainfall and reduces the probability of extreme precipitation. During MJO phases 6–1, however, an anomalous cyclonic circulation dominates the western North Pacific and inherently suppresses precipitation over SC irrespective of the SPV background (Figure S7). This contrast further underscores the strict phase dependence of the SPV–extreme precipitation linkage.

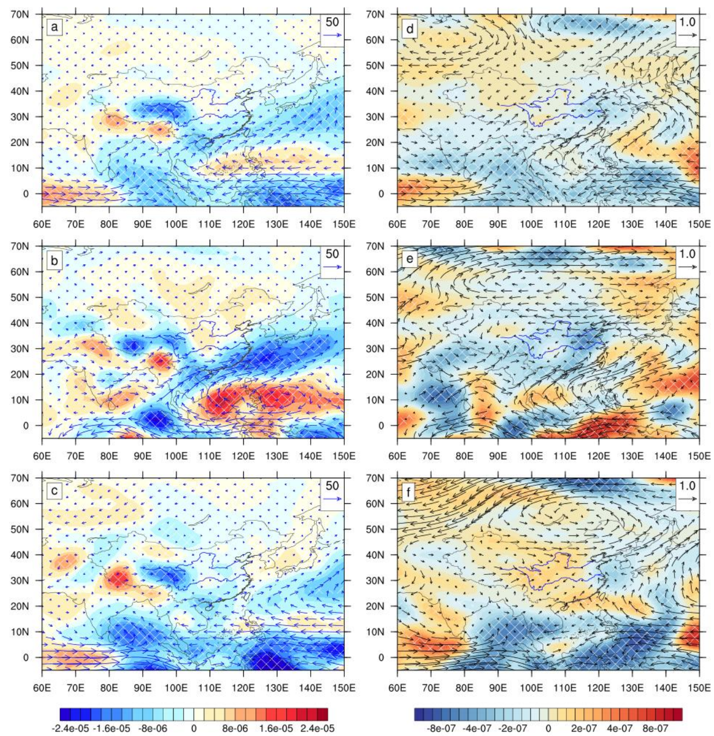

Figure 3 | Circulation responses under the synergistic impacts of ESSPV and MJO phases 2–5. a–c. Composites of vertically integrated (surface to 300 hPa) water vapor fluxes (vectors, unit: kg m^{-1} s^{-1}) and their divergence (shading, unit: kg m^{-2} s^{-1}) during MJO phases 2–5 for (a) all winters, (b) ESSPV winters, and (c) EWSPV winters. **d–f**. Same as **a–c**, but for 850-hPa

https://doi.org/10.5194/egusphere-2026-4214
Preprint. Discussion started: 11 August 2026

horizontal winds (vectors, unit: m s^{-1}) and their divergence (shading, unit: s^{-1}). White meshes indicate significant anomalies at the 95% confidence level.

5 CMIP6 validation of the MJO-dependent SPV–extreme precipitation linkage

To validate the gatekeeping role of the MJO, historical simulations from 27 CMIP6 coupled climate models are further analyzed (see Methods, Table S1). We first quantify each model's ability to reproduce the observed SPV–SC extreme precipitation linkage using two metrics: (1) the composite difference in SC R90 between ESSPV and EWSPV winters, and (2) the temporal correlation coefficient between SC R90 and the ESSPV index (Figure 4a). The model ranking based on the composite difference is broadly consistent with the correlation results: models with an ESSPV–more (less) SC extreme precipitation composite difference correspond to a more negative (positive) correlation coefficient. Given the critical role of the MJO phases 2–5-associated western North Pacific anticyclone revealed in Figure 3, we further evaluate each model's skill in simulating this anticyclone and the MJO itself. Notably, the ESSPV–SC extreme precipitation ranking does not closely align with model performance in reproducing the MJO overall, but is strongly tied to the fidelity of the anticyclone simulation. Models with superior simulation of this anticyclone exhibit a tighter positive linkage between the ESSPV and amplified SC R90, whereas those that reverse or fail to capture the observed SPV–SC extreme precipitation linkage consistently show poor anticyclone representation.

Based on these metrics, we select the 10 best-performing models in simulating the MJO phases 2–5-associated western North Pacific anticyclone (denoted as MJO-MME1) and the 10 poorest-performing models (denoted as MJO-MME2). Independently, we select the 10 models that reproduce the strongest observed positive ESSPV–extreme precipitation linkage (denoted as SPV-MME1) and the 10 that most fail to do so (denoted as SPV-MME2). The two sets of selected models overlap considerably: most models that perform well (poorly) in simulating the anticyclone also perform well (poorly) in reproducing the ESSPV–extreme precipitation linkage. We then conduct a statistical analysis of regionally averaged precipitation over SC during MJO phases 2–5 under different SPV backgrounds for both MME pairs (Figures 4b, c). The precipitation distributions in MJO-MME1 and SPV-MME1 are generally consistent with the observational result (Figure 2c): the 90th percentile of SC precipitation in ESSPV winters is clearly higher than the wintertime 90th percentile threshold, whereas in EWSPV winters it falls below the threshold; additionally, the 75th percentile, 50th percentile, and mean precipitation are all notably higher under ESSPV than under EWSPV. In both MJO-MME2 and SPV-MME2, by contrast, the precipitation difference between ESSPV and EWSPV winters is nearly opposite to the observed pattern, yielding a spurious SPV–SC extreme precipitation relationship.

The dynamical mechanisms underlying these contrasts are further validated by compositing the differences in atmospheric circulation and moisture fields between the two MME pairs (Figures 4d–g). Taking MJO-MME as an example, relative to MJO-MME2, MJO-MME1 exhibits a more pronounced anomalous anticyclone over the western North Pacific, which drives

https://doi.org/10.5194/egusphere-2026-4214
Preprint. Discussion started: 11 August 2026

sufficient southwesterly moisture transport toward SC, together with a stronger ESSPV-associated anomalous anticyclone over eastern Siberia, which delivers cold northeasterly flow that increases precipitation efficiency and favors extreme rainfall. These circulation contrasts align closely with the observational patterns in Figure 3, and collectively explain why the two model ensembles produce opposite ESSPV–SC extreme precipitation linkages. The SPV-MME comparison yields consistent results. Taken together, the CMIP6 results confirm that a clear ESSPV influence on SC extreme precipitation requires the coexistence of two pathways: the high-latitude route, whereby the ESSPV-induced anticyclone north of SC advects cold air southward to confront warm moist air, and the tropical route, whereby the MJO phases 2–5-driven western North Pacific anticyclone provides sufficient moisture that cannot be established without the MJO. The stark contrast between the two MME pairs prominently highlights this low-latitude anticyclonic circulation, underscoring its critical role in supplying both the moisture and the convergent wind field necessary for vertical motion. Given that the MJO-MME groups differ little in their simulation of the ESSPV background and its coupling with the WQBO (Figure S9), these results firmly validate that the MJO is the decisive factor determining whether a model can capture the ESSPV–extreme precipitation linkage over SC.

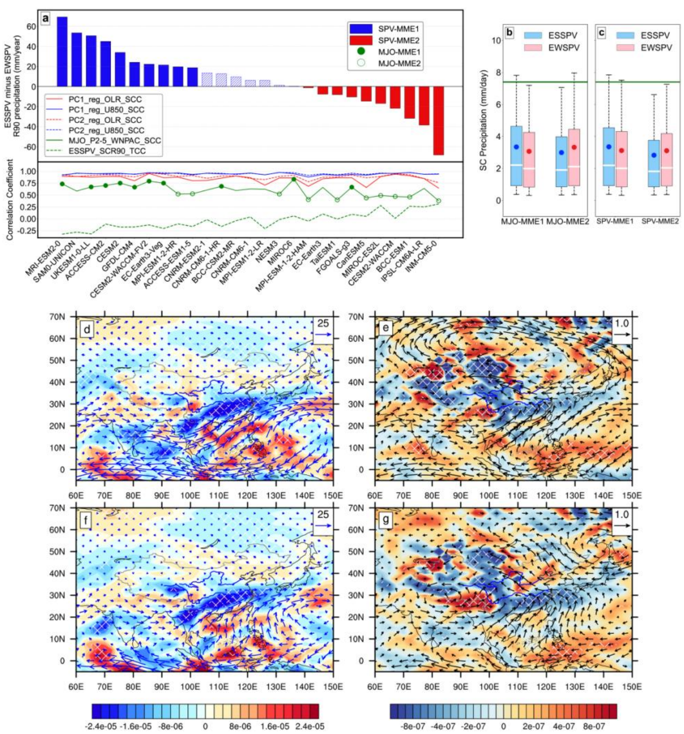

Figure 4 | CMIP6 model validation of the MJO-dependent SPV–extreme precipitation linkage. a. Bar charts denote composite differences of NDJFM-accumulated R90 regionally averaged over SC between ESSPV and EWSPV winters across 27 CMIP6 models (unit: mm). Blue (red) solid bars indicate the 10 models selected for SPV-MME1 (SPV-MME2). The green

https://doi.org/10.5194/egusphere-2026-4214
Preprint. Discussion started: 11 August 2026

solid line denotes the spatial pattern correlation coefficient between each model's MJO phases 2–5-associated western North Pacific anticyclone (defined by the combined OLR and 850-hPa wind pattern over 0°–30°N, 100°–150°E) and the observed counterpart. Green solid (hollow) circles indicate the 10 models selected for MJO-MME1 (MJO-MME2). The green dashed line denotes the temporal correlation coefficient between the winter-mean ESSPV index and SC R90 for each model. Red (blue) lines represent the spatial pattern correlation coefficient between model-derived and observational Hovmöller diagrams (constructed from PC1 and PC2 of OLR and 850-hPa zonal wind anomalies; see Figure S8), with solid (dashed) lines corresponding to PC1 (PC2). **b.** Probability density distributions of daily precipitation (unit: mm day^{-1}) in SC during MJO phases 2–5 in ESSPV (blue) and EWSPV (red) winters for MJO-MME1 and MJO-MME2. Box bounds indicate the 10th, 25th, 50th, 75th, and 90th percentiles; dots indicate the mean. The green solid line marks the observational 90th percentile threshold (approximately 7.4 mm day^{-1}). **c.** Same as **b**, but for SPV-MME1 and SPV-MME2. **d**. Composite differences of vertically integrated (surface to 250 hPa) water vapor fluxes (vectors, unit: kg m^{-1} s^{-1}) and their divergence (shading, unit: kg m^{-2} s^{-1}) between ESSPV and EWSPV winters during MJO phases 2–5 for MJO-MME1 minus MJO-MME2. **e**. Same as **c**, but for 850-hPa horizontal winds (vectors, unit: m s^{-1}) and their divergence (shading, unit: s^{-1}). Meshes indicate significant anomalies at the 95% confidence level. **f–g**. Same as **d–e**, but for SPV-MME1 minus SPV-MME2.

6 Conclusion and discussion

In this study, we defined the longitudinal displacement of the SPV to examine its modulatory effect on extreme precipitation over SC. Under the ESSPV (EWSPV) background, SC extreme precipitation tends to be increased (decreased), yet this linkage is statistically modest. Two factors contribute to this fragility. First, the ESSPV is a seasonal-mean background state that, while favorable for steering cold air southward, does not directly drive moisture transport. Second, a seasonal-mean background alone cannot explain why extreme rainfall events, as transient weather processes, occur on some occasions but not others under the same background. Integration of the MJO, however, reveals that this modulation is not ubiquitous but concentrated in MJO phases 2–5, indicating a distinct phase dependence of the SPV–extreme precipitation relationship on the MJO (Figure 5). When the ESSPV background coincides with MJO phases 2–5, two pathways synergistically enhance extreme precipitation. At high latitudes, the SPV-induced anticyclone north of SC advects cold northeasterly flow, strengthening the thermal contrast between cold northern air and warm moist southern air, which favors wind convergence and sustained upward motion. At low latitudes, the WQBO-associated westerlies, linked to the ESSPV via the Holton–Tan effect, amplify the MJO-induced southwesterly wind anomalies and enhance low-latitude moisture transport toward SC from the western North Pacific anticyclone. The synergy of these multi-latitude pathways creates optimal conditions for SC extreme precipitation. CMIP6 model simulations further validate the robustness of this mechanism: models that more accurately reproduce the MJO phases 2–5-associated western North Pacific anticyclone tend to better capture the negative ESSPV–SC extreme precipitation correlation on the winter-mean timescale, with the inter-model relationship exceeding the 95% significance level. These findings

https://doi.org/10.5194/egusphere-2026-4214
Preprint. Discussion started: 11 August 2026

converge on a central fact that the MJO is the critical key that unlocks the SPV–SC extreme precipitation linkage.

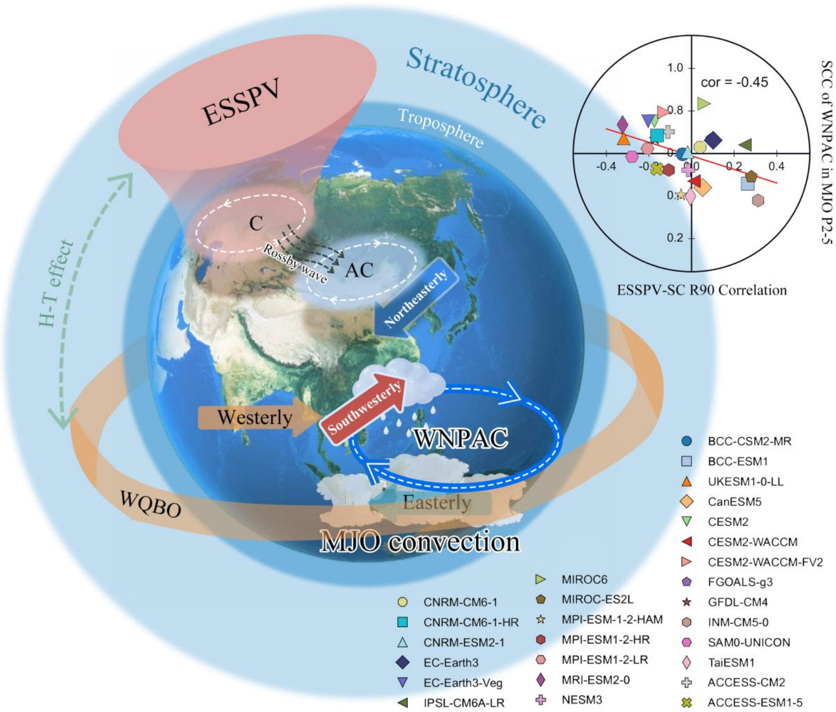

Figure 5 | Schematic diagram of the physical mechanism underlying the SPV–MJO synergistic modulation of extreme precipitation over SC, with attached scatter plot of the spatial pattern correlation coefficient between each CMIP6 model's MJO phases 2–5-associated western North Pacific anticyclone (defined by the combined OLR and 850-hPa wind pattern over 0°–30°N, 100°–150°E) and the observed counterpart, versus the temporal correlation coefficient between each model's winter-mean ESSPV index and SC R90. The red line denotes the cross-model regression, with an inter-model correlation of −0.45 exceeding the 95% significance level.

Our findings highlight the dominant role of the MJO in unlocking the influence of the interannually varying ESSPV background on rainfall extremes in SC. However, several questions remain to be clarified. Although our results can be considered linearly independent of ENSO, other factors, such as Arctic sea ice and oceanic conditions (Nakamura et al., 2016; Kelleher et al., 2020), Eurasian land–atmosphere processes (Ran et al., 2024), and air–sea interactions from the Indian Ocean to the western Pacific (Rao and Ren, 2016; Huang et al., 2021), may also play important roles in modulating SPV–MJO relationships and warrant further investigation. Additionally, this study treats the SPV as a winter-mean background state, yet the SPV itself exhibits pronounced intraseasonal variability. In particular, sudden stratospheric warmings can trigger abrupt SPV collapse, acting as direct precursors to Eurasian cold air outbreaks (Rao et al.,

https://doi.org/10.5194/egusphere-2026-4214
Preprint. Discussion started: 11 August 2026

2019; Lu et al., 2021, 2023). How such SPV intraseasonal processes synergize with the MJO to trigger extreme precipitation remains an open question. Finally, given that the SPV and MJO jointly drive extreme precipitation through two distinct pathways from high and low latitudes, translating this mechanistic understanding into improved subseasonal-to-seasonal prediction of extreme precipitation represents an important challenge for future work (Garfinkel et al., 2012; Garfinkel and Schwartz, 2017). Given these implications, we emphasize the importance of closely monitoring SPV states and MJO signals in future climate projections, encompassing both mid-to-high and low latitudes, with substantial value for formulating disaster prevention and mitigation policies.

Code and data availability

All datasets in this study are publicly available. The daily GPCP precipitation dataset can be obtained from https://www.ncei.noaa.gov/data/global-precipitation-climatology-project-gpcp-daily/access/. The CN05.1 precipitation dataset can be found at https://ccrc.iap.ac.cn/resource/detail?id=228. The NCEP–DOE reanalysis dataset is accessible via https://psl.noaa.gov/data/gridded/data.ncep.reanalysis2.html. The NOAA interpolated OLR dataset is available from https://psl.noaa.gov/data/gridded/data.olrcdr.interp.html. The ERSST version 5 is available from NOAA (https://www.ncei.noaa.gov/products/extended-reconstructed-sst). All CMIP6 datasets can be accessed via the Earth System Grid Federation (ESGF) Data Portal: https://esgf-node.llnl.gov/projects/cmip6/.

The Python 3.10.9 and software National Center for Atmospheric Research (NCAR) Command Language (NCL; available at http://www.ncl.ucar.edu/) are employed for plotting. The code that supports the findings of this study is available from the corresponding author upon reasonable request.

Author contributions

F.Z. contributed to the conceptualization, methodology, investigation, formal analysis, project supervision, and manuscript revision. S.H. contributed to the methodology, investigation, formal analysis, visualization, and original draft. Z.Y. contributed to the investigation and manuscript revision. T.H. and D.H. contributed to the methodology and manuscript revision. All co-authors contributed to the discussion of the results.

Competing interests

The authors declare that they have no conflict of interest.

Acknowledgements

This work was jointly supported by the National Natural Science Foundation of China (No. 42394125), the National Key R&D Program of China (No. 2024YFC3013100), the Jianghuai Meteorological Joint Project of Anhui Natural Science Foundation (No. 2408055UQ004).

References

https://doi.org/10.5194/egusphere-2026-4214
Preprint. Discussion started: 11 August 2026

Adler, R., Sapiano, M., Huffman, G., Wang, J., and Gu, G.: The Global Precipitation Climatology Project (GPCP) Monthly analysis (new version 2.3) and a review of 2017 global precipitation, Atmosphere, 9, https://doi.org/10.3390/atmos9040138, 2018.

Alexander, M., Bladé, I., Newman, M., Lanzante, J., Lau, N. et al.: The atmospheric bridge: The influence of ENSO teleconnections on air–sea interaction over the global oceans, J. Clim., 15, 2205–2231, https://doi./10.1175/1520-0442(2002)015<2205:TABTIO>2.0.CO, 2002a.

Alexander, M., Scott, J.: The influence of ENSO on air-sea interaction in the Atlantic, Geophys. Res. Lett., 29, https://doi./10.1029/2001GL014347, 2002b.

Baldwin, M., Ayarzagüena, B., Birner, T., Butchart, N., Butler, A. et al.: Sudden stratospheric warmings, Rev. Geophys., 59, e2020RG000708, https://doi.org/10.1029/2020RG000708, 2021.

Bao, Q., Yang, J., Liu, Y., Wu, G., and Wang, B.: Roles of anomalous Tibetan Plateau warming on the severe 2008 winter storm in central–southern China, Mon. Weather Rev, 138, 2375–2384, https://doi./10.1175/2009MWR2950.1, 2010.

Chen, X., Li, C., Li, L., Yu, P., and Yang, M.: Interannual variations of the influences of MJO on winter rainfall in southern China, Environ. Res. Lett., 15, 114011, https://doi./10.1088/1748-9326 /abb7b0, 2020.

DeFlorio, M., Waliser, D., Ralph, F., et al.: Experimental subseasonal-to-seasonal (S2S) forecasting of atmospheric rivers over the western United States, J. Geophys. Res.:Atmos., 124, 11242–11265, https://doi./10.1029/2019JD031200, 2019.

Dey, A., Chattopadhyay, R., Sahai, A., Mandal, R., Joseph, S., Phani, R., and Pattanaik, D.: MJO prediction skill using IITM extended range prediction system and comparison with ECMWF S2S, Pure Appl. Geophys., 177, 5067–5079, https://doi./10.1007/s00024-020-02487-z, 2020.

Eyring, V., Bony, S., Meehl, G., Senior, C., Bjornet,S. et al.: Overview of the Coupled Model Intercomparison Project Phase 6 (CMIP6) experimental design and organization, Geosci. Model Dev., 9, 1937–1958, https://doi./10.5194/gmd-9-1937-2016, 2016.

Gao, H., and Yang, S.: A severe drought event in northern China in winter 2008–2009 and the possible influences of La Niña and Tibetan Plateau, J. Geophys. Res.:Atmos., 114, https://doi./10.1029/2009JD012430, 2009.

Garfinkel, C., and Schwartz, C.: MJO-Related tropical convection anomalies lead to more accurate stratospheric vortex variability in subseasonal forecast models, Geophys. Res. Lett., 44, 10,054–10,062, https://doi.org/10.1002/2017GL074470, 2017.

Garfinkel, C., Benedict, J., and Maloney, E.: Impact of the MJO on the boreal winter extratropical circulation, Geophys. Res. Lett., 41, 6055–6062, https://doi.org/10.1002/2014GL061094, 2014.

Garfinkel, C., Feldstein, S., Waugh, D., et al.: Observed connection between stratospheric sudden warmings and the Madden–Julian Oscillation, Geophys. Res. Lett., 39, https://doi.org/10.1029/2012GL053144, 2012.

Green, M., and Furtado, J.: Evaluating the joint influence of the Madden–Julian oscillation and the stratospheric polar vortex on weather patterns in the Northern hemisphere, J. Geophys. Res.:Atmos., 124, 11693–11709 , https://doi.org/10.1029/2019JD030771, 2019.

https://doi.org/10.5194/egusphere-2026-4214
Preprint. Discussion started: 11 August 2026

Han, J., and Zhang, R.: Influence of preceding North Atlantic Oscillation on the spring precipitation in the middle and lower reaches of the Yangtze River valley, Int. J. Climatol., 42, 4728–4739, https://doi.org/10.1002/joc.7500, 2022.

He, B., Liu, Y., Wu, G., Wang, Z., and Bao, Q.: The role of air–sea interactions in regulating the thermal effect of the Tibetan–Iranian plateau on the Asian summer monsoon, Clim. Dyn. 52, 4227–4245, https://doi.org/10.1007/s00382-018-4377-y, 2019.

Hu, D., Yang, J., Zhang, H., Mo, R., and Guan, Z.: Influences of stratospheric Arctic vortex on surface air temperature over Asia. J, Geophys. Res.:Atmos., 129, e2024JD040866, https://doi.org/10.1029/2024JD040866, 2024.

Hu, D., Liu, M., Guan, Z., Tian, W., and Yin, Z.: Longer duration of extreme cold events over East Asia affected by the stratospheric polar vortex extension, J. Geophys. Res.:Atmos., 130, e2024JD042299 , https://doi.org/10.1029/2024JD042299, 2025.

Huang, B., Thorne, P., Banzon, V., Boyer, T.: Chepurin, G. et al.: Extended reconstructed sea surface temperature, version 5 (ERSSTv5): upgrades, validations, and intercomparisons, J. Clim., 30, 8179–8205, https://doi.org/10.1175/JCLI-D-16-0836.1, 2017.

Huang, R., Tian, W., Qie, K., et al.: Contrasting effects of Indian Ocean basin and dipole modes on the stratosphere, J. Geophys. Res.:Atmos., 126, e2021JD035156, https://doi.org/10.1029/2021JD035156, 2021.

Huang, R., Xu, Y., Wang, P., and Zhou, L.: The features of the catastrophic flood over the Changjiang River basin during the summer of 1998 and cause exploration (in Chinese), Clim. Environ. Res., 3, 300–313 ,1998.

IPCC.: Climate change 2021: The physical science basis. Contribution of Working Group I to the Sixth Assessment Report of the Intergovernmental Panel on Climate Change, edited by: Masson-Delmotte, V., et al., Cambridge University Press, Cambridge, UK and New York, USA, https://doi.org/10.1017/9781009157896, 2021.

Jia, X., Chen, L., Ren, F., and Li, C.: Impacts of the MJO on winter rainfall and circulation in China, Adv. Atmos. Sci., 28, 521–533, https://doi.org/10.1007/s00376-010-9118-z, 2011.

Kanamitsu, M., Ebisuzaki, W., Woollen, J., Yang, S., Hnilo, J., Fiorino, M., and Potter, G.,:Ncep–doe amip–ii reanalysis (r–2), Bull. Am. Meteorol. Soc., 83, 1631–1644, https://doi.org/10.1175/BAMS-83-11-1631(2002)083<1631:NAR>2.3.CO;2, 2002.

Kelleher, M., Ayarzagüena, B., Screen, J.: Interseasonal connections between the timing of the stratospheric final warming and Arctic sea ice, J. Clim., 33, 3079–3092, https://doi.org/10.1175/JCLI-D-19-0064.1, 2020.

Kim, H., Son, S., Kim, H., Seo, K., and Kang, M.: MJO influence on subseasonal–to–seasonal prediction in the Northern Hemisphere extratropics, J. Clim., 36, 7943–7956, https://doi.org/10.1175/JCLI-D-23-0139.1, 2023.

Liebmann, B., and Smith, C.: Description of a complete (interpolated) outgoing longwave radiation dataset, Bull. Am. Meteorol. Soc., 77, 1275–1277, 1996.

Liu, B., Wu, G., Mao, J., and He, J.: Genesis of the South Asian high and its impact on the Asian summer monsoon onset, J. Clim., 26, 2976–2991, https://doi.org/10.1175/JCLI-D-12-00286.1, 2013.

https://doi.org/10.5194/egusphere-2026-4214
Preprint. Discussion started: 11 August 2026

Liu, C., Tian, B., Li, K., et al.: Northern Hemisphere mid–winter vortex–displacement and vortex–split stratospheric sudden warmings: Influence of the Madden–Julian Oscillation and Quasi–Biennial Oscillation, J. Geophys. Res.:Atmos., 119, 12,599–12,620, https://doi.org/10.1002/2014JD021876, 2014.

Liu, X., Peng, Y., Su, J. and Liu, X.: To identify the forecast skill windows of MJO based on the S2S database, Geophys. Res. Lett., 51, e2024GL109903, https://doi.org/10.1029/2024GL109903, 2024.

Lu, M., Yang, S., Zhu, C., Wang, J., Lin, S., Wei, W., and Fan, H.: Thermal impact of the southern Tibetan Plateau on the southeast Asian summer monsoon and modulation by the tropical Atlantic SST, J. Clim., 36, 1319–1330, https://doi.org/10.1175/JCLI-D-22-0493.1, 2023.

Lu, Q., Rao, J., Liang, Z., et al.: The sudden stratospheric warming in January 2021, Environ. Res. Lett., 16, 084029, https://doi.org/10.1088/1748-9326/ac12f4, 2021.

Lu, Q., Rao, J., Shi, C., et al.: Stratosphere-troposphere coupling during stratospheric extremes in the 2022/23 winter, Weather Clim. Extremes., 42, 100627, https://doi.org/100627,10.1016/j.wace.2023, 2023.

Madden, R., and Julian, P.: Detection of a 40–50 day oscillation in the zonal wind in the tropical Pacific, J. Atmos. Sci., 28, 702–708, https://doi.org/10.1175/1520-0469(1971)028<0702:DOADOI>2.0.CO;2, 1971.

Madden, R., and Julian, P.: Observations of the 40–50–day tropical oscillation—A review, Mon. Weather Rev., 122, 814–837, https://doi.org/10.1175/1520-0493(1994)122<0814:OOTDTO>2.0.CO;2, 1994.

Martin, Z., Son, S., Butler, A., et al.: The influence of the quasi-biennial oscillation on the Madden–Julian oscillation, Nat. Rev. Earth Environ., 2, 477–489, https://doi.org/10.1038/s43017-021-00173-9, 2021.

Nakamura, T., Yamazaki, K., Iwamoto, K., et al.: The stratospheric pathway for Arctic impacts on midlatitude climate, Geophys. Res. Lett., 43, 3494–3501, https://doi.org/10.1002/2016GL068330,2016.

Peng, Y., Liu, X., Su, J., and Liu, X.: Classification analysis of prediction skill among ensemble members in MJO subseasonal predictions—based on the results of the CAMS–CSM subseasonal prediction system, Atmos. Oceanic Sci. Lett., 17, 100469, https://doi.org/10.1016/j.aosl.2024.100469, 2024.

Ran, X., Hu, D., Zhang, Y., et al.: Relationship between the stratospheric Arctic vortex and surface air temperature in the midlatitudes of the Northern Hemisphere, J. Meteorol. Res., 38, 39–52, https://doi.org/10.1007/s13351-024-3072-7, 2024.

Rao, J., Garfinkel, C., Chen, H., and White, I.: The 2019 new year stratospheric sudden warming and its real-time predictions in multiple S2S models, J. Geophys. Res.:Atmos., 124, 11155–11174, https://doi.org/10.1029/2019JD030826, 2019.

Rao, J., Garfinkel, C., Zhang, X., and Lu, Q.: Subseasonal to seasonal (s2s) prediction of continental cold following the sudden stratospheric warming in the 2022/23 winter, Clim. Dyn., 63, https://doi.org/10.1007/s00382-024-07582-8, 2025.

Rao, J. and Ren, R.: A decomposition of ENSO’s impacts on the northern winter stratosphere:

https://doi.org/10.5194/egusphere-2026-4214
Preprint. Discussion started: 11 August 2026

Competing effect of SST forcing in the tropical Indian Ocean, Clim. Dyn., 46, 3689–3707, https://doi.org/10.1007/s00382-015-2797-5, 2016.

Rivoire, P., Martius, O., Naveau, P., et al.: Assessment of subseasonal–to–seasonal (S2S) ensemble extreme precipitation forecast skill over Europe, Nat. Hazards Earth Syst. Sci., 23, 2857–2871, https://doi.org/10.5194/nhess-23-2857-2023, 2023.

Schreck III, C.: Global survey of the MJO and extreme precipitation, Geophys. Res. Lett., 48, e2021GL094691, https://doi.org/10.1029/2021GL094691, 2021.

Shimizu, M., Ambrizzi, T., Liebmann, B.: Extreme precipitation events and their relationship with ENSO and MJO phases over northern South America, Int. J. Climatol., 37, 2977–2989, https://doi.org/10.1002/joc.48932017.

Takaya, K. and Nakamura, H.: A formulation of a phase–independent wave–activity flux for stationary and migratory quasigeostrophic eddies on a zonally varying basic flow, J. Atmos. Sci., 58, 608–627, https://doi.org/10.1175/1520-0469(2001)058<0608:AFOAPI>2.0.CO;2, 2001.

Wang, Q., Duan, A., Dai, A., Cao, S., Zhou, A., Gao, Y., et al.: Arctic stratospheric polar vortex collapse amplified South China extreme rainfall in April 2024, npj Clim. Atmos. Sci., 8, 217, https://doi.org/10.1038/s41612-025-01107-8, 2025.

Wang, Y., Ren, H., Wei, Y., Jin, F., Ren, P., Gao, L., and Wu, J.: MJO phase swings modulate the recurring latitudinal shifts of the 2020 extreme summer-monsoon rainfall around Yangtse, J, Geophys. Res.:Atmos., 127, e2021JD036011, https://doi.org/10.1029/2021JD036011, 2022.

Wei, W., Zhang, R., Wen, M., Kim, B., and Nam, J.: Interannual variation of the South Asian high and its relation with Indian and East Asian summer monsoon rainfall, J. Clim., 28, 2623–2634, https://doi.org/10.1175/JCLI-D-14-00454.1, 2015.

Wu, J. and Gao, X.: A gridded daily observation dataset over China region and comparison with the other datasets, Chin. J. Geophys., 56, 1102–1111, https://doi.org10.6038/cjg20130406, 2013.

Yao, Y., Lin, H., and Wu, Q.: Subseasonal variability of precipitation in China during boreal winter, J. Clim., 28(16), 6548–6559, https://doi.org/10.1175/JCLI-D-15-0033.1, 2015.

Yin, Y., Chen, H., Zhai, P., Xu, C. Y., and Ma, H.: Characteristics of summer extreme precipitation in the Huai River basin and their relationship with East Asia summer monsoon during 1960–2014, Int. J. Climatol., 39, 1555–1570, https://doi.org/10.1002/joc.5900, 2019.

Yu, Y., Cai M., Shi C. and Ren R.: On the linkage among strong stratospheric mass circulation, stratospheric sudden warming, and cold weather events, Mon. Wea Rev., 146, 2717–2739, https://doi.org/10.1175/MWR-D-18-0110.1, 2018.

Yu, Y. and Ren, R.: Understanding the variation of stratosphere–troposphere coupling during stratospheric northern annular mode events from a mass circulation perspective, Clim. Dyn., 53, 5141–5164, https://doi.org/10.1007/s00382-019-04675-7, 2019.

Zhang, J., Zheng, H., Xu, M., Yin, Q., Zhao, S., Tian, W., and Yang, Z.: Impacts of stratospheric polar vortex changes on wintertime precipitation over the northern hemisphere, Clim. Dyn., 58, https://doi.org/10.1007/s00382-022-06167-7, 2022.

Zhang, Q., Zheng, Y., Singh, V., Luo, M., and Xie, Z.: Summer extreme precipitation in eastern

https://doi.org/10.5194/egusphere-2026-4214
Preprint. Discussion started: 11 August 2026

China: Mechanisms and impacts, J. Geophys. Res.:Atmos., 122, 2766–2778, https://doi.org/10.1002/2016JD025913, 2017.

Zhang, R.: Changes in East Asian summer monsoon and summer rainfall over eastern China during recent decades, Sci. Bull., 60, 1222–1224, https://doi.org/10.1007/s11434-015-0824-x, 2015.

Zhang, R., Tian, W., Zhang, J., Huang, J., Xie, F., and Xu, M.: The corresponding tropospheric environments during downward–extending and nondownward–extending events of stratospheric northern annular mode anomalies, J. Clim., 32, 1857–1873, https://doi.org/10.1175/JCLI-D-18-0574.1, 2019.

Zhang, W., Xiang, B., Tseng, K., et al.: Subseasonal–to–seasonal (S2S) prediction of atmospheric rivers in the Northern Winter, npj Clim. Atmos. Sci., 7, https://doi.org/10.1038/s41612-024-00827-7, 2024.

Zhang, X., Alexander, L., Hegerl, G., Jones, P., Tank, A., Peterson, T., et al.: Indices for monitoring changes in extremes based on daily temperature and precipitation data, Wiley Interdiscip, Rev. Clim. Change., 2, 851–870, https://doi.org/10.1029/2019JD032263, 2011.

Zhang, Y., Yin, Z., Tian, W., et al.: Stratospheric precursor induces wintertime phase reversal of the "warm Arctic–cold Eurasia" pattern, Nat. Commun., 17, https://doi.org/10.1038/s41467-026-70100-3, 2026.

Zhou, F., Siseho, C., Liu, M., Zhang, D., and Zhang, H.: Joint impacts of the North african and the western pacific subtropical highs on summer precipitation over the Tibetan plateau, J. Clim., 37, 3825–3846, https://doi.org/10.1175/JCLI-D-23-0560.1, 2024.

Zhou, Z., Xie, S., and Zhang, R.: Historic Yangtze flooding of 2020 tied to extreme Indian Ocean conditions, Proc, Natl. Acad. Sci., India., 118, e2022255118, https://doi.org/10.1073/pnas.2022255118, 2021.

Zhu, K., and Xue, M.: Evaluation of WRF-based convection-permitting multi-physics ensemble forecasts over China for an extreme rainfall event on July 21, 2012 in Beijing, Adv. Atmos. Sci., 33, 1240–1258, https://doi.org/10.1007/s00376-016-6202-z, 2016.

Zhu, Z., Feng, Y., Jiang, W., Lu, R., and Yang, Y.: The compound impacts of sea surface temperature modes in the Indian and North Atlantic oceans on the extreme precipitation days in the Yangtze River Basin, Clim. Dyn., 61, 3327–3341, https://doi.org/10.1007/s00382-023-06733-7, 2024.